


## Research Article

# In Situ Synthesis of Zeolites in Solidified Fly Ash/Cement Matrices with High Na Content: Products, Pore Structure, and Leaching Behavior

Zhao Zheng <sup>1,2</sup>, Zhitao Bao,<sup>1,2</sup> Qingyi Wang,<sup>1,2</sup> and Yuxiang Li<sup>3</sup>

<sup>1</sup>Shock and Vibration of Engineering Materials and Structures Key Laboratory of Sichuan Province, Southwest University of Science and Technology, Mianyang 621010, China

<sup>2</sup>School of Civil Engineering and Architecture, Southwest University of Science and Technology, Mianyang 621010, China

<sup>3</sup>School of Materials Science and Engineering, Southwest University of Science and Technology, Mianyang 621010, China

Correspondence should be addressed to Zhao Zheng; zhengzhao@swust.edu.cn

Received 31 August 2022; Revised 18 October 2022; Accepted 29 October 2022; Published 8 November 2022

Academic Editor: Zhigang Zang

Copyright © 2022 Zhao Zheng et al. This is an open access article distributed under the Creative Commons Attribution License, which permits unrestricted use, distribution, and reproduction in any medium, provided the original work is properly cited.

Due to its high retention capacity and well durability, fly ash-based geopolymers rich of zeolites are considered to be potential solidified materials for low- and intermediate-level radioactive waste stream. This study mainly focused on the phase transformation, pore structure, and leaching characteristic of  $\text{Sr}^{2+}$  and  $\text{Cs}^+$  in solidified fly ash/cement matrices under different sodium hydroxide contents or sodium nitrate concentrations after thermal curing of 28 d. The results obtained from the experiments indicated that the geopolymers prepared from pure fly ash had the potential to transform into ordered structures at high temperatures of 90°C instead of room temperature, such as Na-P1 zeolite and chabazite. With the increase in sodium hydroxide contents, more sodium nitrate participated in the reaction to form a zeolite phase in solidified fly ash/cement matrices, while the coexistence phenomenon of chabazite and Na-P1 zeolite appeared under the condition of high sodium hydroxide contents of more than 5%. Just a proper number of zeolites can effectively inhibit the leaching of radionuclides  $\text{Sr}^{2+}$ , as too many zeolites would lead to the increase in porosity, which was harmful to the retention of radionuclides. Solidified fly ash/cement matrices at a sodium hydroxide content of 5% or at a sodium nitrate concentration of 300 g/L obtained the lowest cumulative leaching fraction of  $\text{Sr}^{2+}$ . Moreover, sodium hydroxide increased the cumulative leaching fraction of  $\text{Cs}^+$  which reversely decreased significantly with the increase in sodium nitrate concentrations.

## 1. Introduction

Intermedium- and low-level radioactive waste (ILLRW) stream is a solution with high content of salts and alkalis produced in the postprocessing of spent fuels, which accounts for more than 95% of the total radioactive waste stream [1]. Cement solidification technology is widely used in the treatment and disposal of ILLRW stream due to its economic raw materials, simple technology, and high adsorption capacity of C-S-H and ettringite on radionuclides [2, 3]. However, the large amount of mesopores and macropores in solidified cement matrices (SCMs) and weak acid resistance resulted in the poor stability of the SCM under complex geological conditions (water, heat, and chemistry

[4]. The occurrence state of radionuclides in the SCM is mainly physical inclusion and chemical adsorption. It is easy to cause desorption and leaching of simulated radionuclides in the process of decalcification and degradation of the SCM. Therefore, cement solidification technology also has certain limitations in the treatment of ILLW stream. Fortunately, alkali-activated geopolymers have stronger acid resistance than cement, although they are both alkaline materials [5]. Moreover, the reaction products of geopolymers at normal temperature are three-dimensional network N-A-S-H gels with similar zeolitic structures, while zeolite crystals get formed at high temperature (60–200°C) curing [6]. Geopolymers have variable phase structures and phase compositions, but generated gels and zeolites can effectively

adsorb simulated radionuclides, which remedy the short board of cement solidification technology and improve the retention efficiency and long-term stability [7, 8]. Thus, solidified fly ash/cement matrices (SFCMs) are considered potential systems to immobilization of radionuclides by taking advantage of both cement and geopolymer, especially in mass immobilization engineering, which needs rather high content of fly ash to decrease hydration heat.

As the chemical properties of Cs are very similar to those of alkali metal ions, it prefers to participate in the formation of geopolymers. Cs is more likely to be adsorbed on N-(C)-A-S-H gels than on C-A-S-H gels [9] and plays a vital role of electricity balance in the silicoaluminate network [10]. The adsorption kinetics of Cs in geopolymers also conformed to the pseudofirst-order and pseudosecond-order kinetic models, which also demonstrated that physical and chemical adsorption mechanisms dominated the whole adsorption process [11]. Jang et al. [12] studied the physical shielding effect of Portland cement, fly ash, as well as slag-based geopolymers on the leaching characteristic of Cs, and the effect indicated that the leaching of Cs in fly ash-based geopolymers (FABGs) was the lowest due to the dense pore structure. Li et al. [13] suggested that the addition of Cs had no obvious impact on the structure and composition of FABG, but FABG had better solidification ability and mechanical properties than cement.

In order to further improve the retention ability of geopolymers, modification and functionalization of geopolymers have been studied [14, 15]. However, the introduction of other substances may have a negative impact on the durability of geopolymers and increase the complexity of the production process, which is not suitable for large-scale production lines. In contrast, it is more effective and simpler to enhance the retention ability of geopolymers for simulated nuclides by increasing the curing temperature to form in situ zeolite phases. Many in situ synthesis methods have been applied in the formation of new functional materials, such as photocatalysis materials [16, 17], nanostructures materials [18–20], and optical materials [21]. The methods used in the above materials, including hydrothermal synthesis, room temperature synthesis, and catalytic synthesis, can provide strong guidance for the in situ synthesis of zeolites in geopolymers.

There are cross-linked channels in the three-dimensional network structure of zeolites, and the pore size is 2.5–5.0 Å [22]. This special structure enables zeolites to have high ion exchange capacity and selectivity for Sr and Cs. In previous studies, a variety of zeolites were used to adsorb Sr and Cs, such as Na-P1 zeolite, chabazite, Linde-A zeolite, faujasite zeolite, and mordenite. Baek et al. [23] and Aono et al. [24] showed that chabazite had the highest adsorption selectivity for Cs, while Munthali et al. [25] showed that Linde-A zeolite had the highest adsorption selectivity for Sr. Thus, N-A-S-H gels and zeolites have excellent selective adsorption properties for Sr and Cs, which can effectively improve the immobilization ability of the matrix.

Alkali can activate fly ash to produce the zeolite phase at high temperature, especially chabazite and P-type zeolite, which have good adsorption and retention effects on

simulated radionuclides of Sr and Cs [15, 26, 27]. Due to the limitation of the ILLRW immobilization process, the way of adding sodium silicate solution is not easy to implement, while the way of adding sodium hydroxide powers is relatively simple. Therefore, this paper mainly studied the influence of sodium hydroxide as alkali activators on the formation of the zeolite phase from fly ash at room temperature or thermal curing. Moreover, the phase transformation, pore structure, and leaching characteristic of  $\text{Sr}^{2+}$  and  $\text{Cs}^+$  in the SFCM under different sodium hydroxide contents and sodium nitrate concentrations have also been further researched. This study was further researched on the performance of the SFCM on the retention of radionuclides based on the previous study [28], which is meaningful to unveil the stability of radionuclides in different zones of mass immobilization matrices.

## 2. Materials and Methods

**2.1. Materials.** Ordinary Portland cement P O 42.5R (China standard: GB 175–2007) and fly ash with a low content of Ca are used in this study, and the detailed composition and particle size can be seen in the previous study [29]. Analytical reagent-grade sodium nitrate, strontium nitrate, cesium nitrate, and sodium hydroxide were purchased from the chemical reagent company.

**2.2. Preparation of Samples.** FABG is prepared by mixing fly ash, sodium hydroxide, and water. According to the previous study on synthesis of zeolites [27], sodium hydroxide was dissolved in water before stirring, and contents (mass ratio of sodium hydroxide to fly ash) were 10%, 15%, and 20%, respectively. The mass ratio of water to fly ash in FABG was constant at 0.4. After stirring for 5 min, fresh pastes were poured into  $20 \times 20 \times 20 \text{ mm}^3$  steel molds and then vibrated for 1 min to remove air bubbles. The synthesis temperature was selected at  $90^\circ\text{C}$  [27]. The samples were demolded after 5 h of curing and then continued to be cured at  $90^\circ\text{C}$  for 28 d. After that, the samples were smashed into small fragments or ground into powder for characterization.

Fly ash/cement paste (FCP) curing at  $20^\circ\text{C}$  and SFCM curing at  $20^\circ\text{C}$  or  $90^\circ\text{C}$  were also prepared as per the method described above. Sodium hydroxide and sodium nitrate were dissolved in water before stirring. The concentration of sodium nitrate was between 0 and 500 g/L, while the sodium hydroxide content was between 0.82% and 10% (calculated as the mass ratio of  $\text{Na}_2\text{O}$  to fly ash and cement). Table 1 lists the mixture proportions of the SFCM. As the salt concentration of normal ILLRW was always around 300 g/L and the sodium hydroxide content was around 0.82%, sodium nitrate of 300 g/L was selected for samples 7–10. The concentrations of  $\text{Cs}^+$  and  $\text{Sr}^{2+}$  (mass ratio of radionuclide to cement and fly ash) in all the SFCMs were 0.4% and 0.8%, respectively.

**2.3. Leaching Experiment.** The leaching experiment was conducted based on the Chinese standard GB/T 7023-2011. The leaching agent is an  $\text{NH}_4\text{Cl}$  solution of 0.6 mol/L, and

TABLE 1: The mixture proportions of the SFCM.

Samples	Cement (g)	Fly ash (g)	W/C (mass ratio)	C <sub>NaNO<sub>3</sub></sub> (g/L)	Solution (g)	NaOH (%)
1	15	85	0.4	0	40	5
2	15	85	0.4	100	44.15	5
3	15	85	0.4	200	48.48	5
4	15	85	0.4	300	53.55	5
5	15	85	0.4	400	58.94	5
6	15	85	0.4	500	64.90	5
7	15	85	0.4	300	53.55	0
8	15	85	0.4	300	53.55	0.82
9	15	85	0.4	300	53.55	2.5
10	15	85	0.4	300	53.55	7.5
11	15	85	0.4	300	53.55	10

the volume ratio of solidified fly ash/cement matrices to NH<sub>4</sub>Cl solution is 1:30. The leaching experiment was conducted at 25 ± 2°C, while the leaching agent was refreshed at the leaching period ranging from 2 h to 28 d, respectively. The leaching fraction (LF, cm d<sup>-1</sup>) and the cumulative leaching fraction (CLF, cm) were obtained by following the formations described in the previous study [28].

**2.4. Characterization.** The crystalline phases in solidified matrices were detected by X-ray diffractometry (XRD) (DMAX1400, Rigaku, Japan). A scanning electron microscope (SEM) (Ultra55, Carl-Zeiss, Germany) was used to analyze the morphology of the solidified matrices. The change in Si-O-T (T=Si and Al) bonds was examined through the infrared spectra (IR) (Spectrum One Autoima, PE, USA). The pore structure of samples with a diameter of ~4 mm was determined by mercury intrusion porosimetry (MIP) (AutoPore IV9500, Micromeritics, USA). The concentrations of cations in leaching solutions were detected by inductively coupled plasma optical emission spectroscopy (ICP) (iCAP 7000, Thermo Fisher Scientific, USA), and the results were obtained from the average value of three test data.

### 3. Results and Discussion

**3.1. Hydration Characteristics of FCP at Room Temperature.** Figure 1 displays the hydration exothermic curves of FCP under different sodium nitrate concentrations at 20°C. As seen in Figure 1(a), the hydration of FCP is delayed with the increase in sodium nitrate concentrations. The starting time of an acceleration period is also delayed, while the duration of an acceleration period is prolonged, as seen in the first exothermic peak in the zone of peak I. It is worth noting that FCP has no obvious second exothermic peak under the condition of pure water. However, at a sodium nitrate concentration of >100 g/L, the second exothermic peak becomes higher and higher. The second exothermic peak is also delayed with increasing sodium nitrate concentrations, as seen in the zone of peak II. As seen in Figure 1(b), at the hydration age of 3 d, the normalized heat of FCP under pure water begins to increase slowly. As most of the single phase of cement was hydrated completely in the pure water at 3 d,

the rate of hydration decreased obviously (Figure 1(a)). However, the normalized heat of FCP in sodium nitrate solution still increased sharply as sodium nitrate restrained the hydration of cement in the first few days [28]. When the hydration age is 7 d, the normalized heat of FCP in pure water is between that in sodium nitrate concentrations of 300 g/L and 500 g/L. However, the normalized heat of FCP in pure water is close to that in 200 g/L of sodium nitrate at the hydration age of 14 d.

As seen in Figure 2, high concentrations of sodium nitrate (≥ 300 g/L) prevent the hydration of C<sub>2</sub>S and C<sub>3</sub>S in the SFCM and decreases the content of Ca(OH)<sub>2</sub>. This is consistent with the conclusions in the previous study on the influence of sodium nitrate on the hydration of Portland cement [28]. The appearance of Peak II (Figure 1) is attributed to the hydration of some residual C<sub>2</sub>S and C<sub>3</sub>S, as well as the hydration of fly ash under the activation of OH<sup>-</sup> and Na<sup>+</sup>.

Figure 3 shows the hydration exothermic curves of FCP with different sodium hydroxide contents at 20°C. As seen in Figure 3(a), the hydration exothermic peak of FCP advances with the increase in sodium hydroxide contents, and the duration time of the acceleration period and the deceleration period is shortened. When the sodium hydroxide content is 5% and 10%, the second exothermic peak of FCP disappears. As seen in Figure 3(b), the normalized heat of FCP increases significantly with the increase in sodium hydroxide contents before the hydration of 1.5 d. After the 3 d of hydration, the normalized heat of FCP with sodium hydroxide is obviously lower than that of the blank sample. The increasing pH by the introduction of NaOH promoted the hydration process of cement at early age [30, 31]. However, owing to the formation of dense products film on cement particles, the hydration degree decreased obviously at a later age [32].

As seen in Figure 4, the addition of sodium hydroxide (<5%) at normal temperature does not significantly change the crystalline products in the SFCM. Only when the sodium hydroxide content is 5% and 10%, a small amount of cancrinite (PDF: 78-2494) and tetranatrolite (PDF: 33-1205) appears in the matrix.

**3.2. In Situ Synthesis of Zeolite Phases from Fly Ash under Thermal Curing.** Figure 5 shows the XRD patterns of FABG with different sodium hydroxide contents after curing at

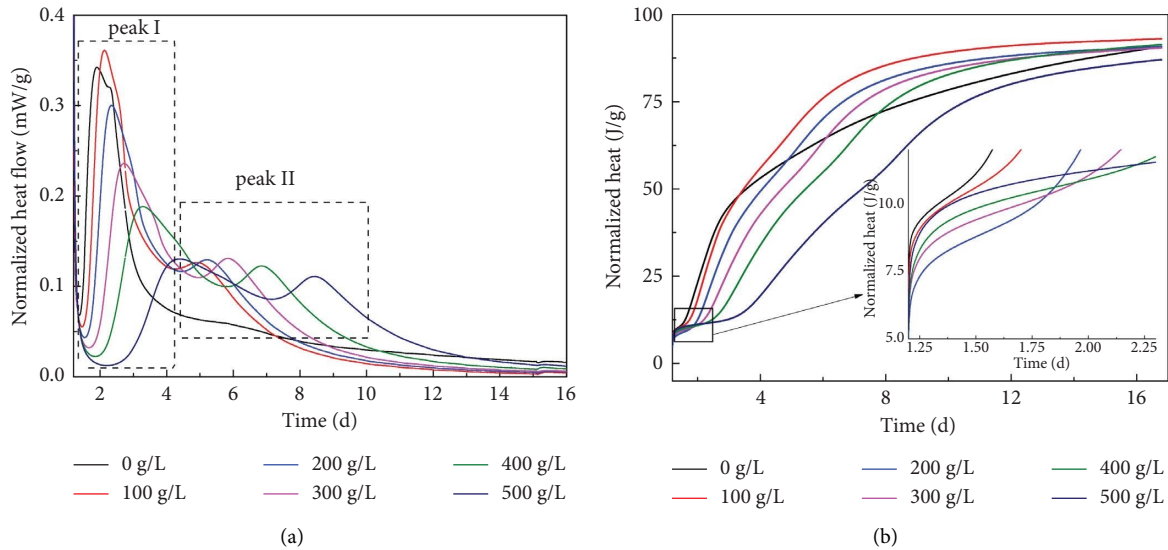


FIGURE 1: The hydration exothermic curves of the SFCM with different sodium nitrate concentrations at 20°C: (a) normalized heat flow; (b) normalized heat.

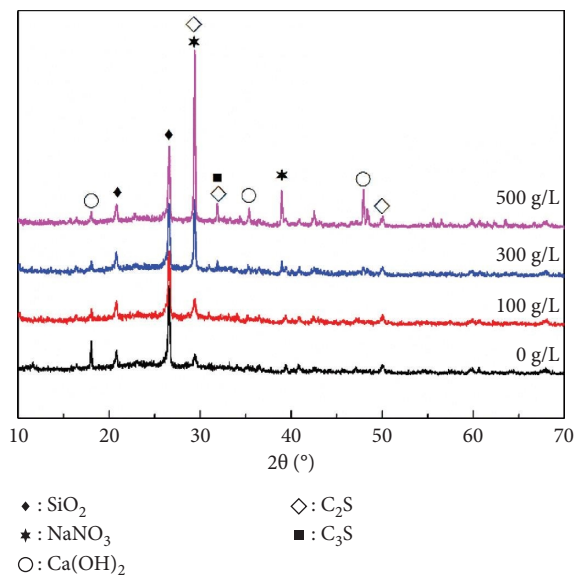


FIGURE 2: The XRD patterns of the SFCM with different concentrations of sodium nitrate after curing at 20°C for 7 d.

90°C. As seen in Figure 5(a), the crystal phase of the FABG matrix with 10% of sodium hydroxide is only silica and mullite after curing at 90°C for 1 d, while there is no new crystal phase. When the sodium hydroxide content increases to 15%, the sodalite phase begins to appear in the matrix. The peak strength of the sodalite phase in the matrix is significantly enhanced at a sodium hydroxide content of 20%, and a new phase of chabazite appears. It can be seen in Figure 5(b) that the kinds of crystalline phases in FABG with different sodium hydroxide contents increase significantly after curing at 90°C for 7 d. When the sodium hydroxide content is 10%, the faujasite phase and the nepheline phase appear in the matrix besides the chabazite phase. However,

the faujasite phase disappears at a sodium hydroxide content of 15%, but the new phase of Na-P1 zeolite appears. At last, the main zeolite phases in the matrix are chabazite, Na-P1 zeolite, and sodalite, while the content of sodium hydroxide is 20%. However, the diffraction peak intensity of the Na-P1 zeolite phase is much lower than that at a sodium hydroxide content of 15%, and the diffraction peak of silica significantly reduces. Figure 5(c) shows that the main crystal phase of FABG with a sodium hydroxide content of 10% is chabazite after curing at 90°C for 28 d. Moreover, there is a small amount of the Na-P1 zeolite phase, and the diffraction peak of silica is obvious. When the sodium hydroxide content increases to 15%, the diffraction peak of silica in the matrix is not obvious, while the diffraction peak intensity of the Na-P1 zeolite phase in the matrix is significantly enhanced. However, the diffraction peak intensity of the Na-P1 zeolite phase reduces at a sodium hydroxide content of 20%. Nevertheless, the main crystalline phase in the matrix is still the chabazite phase.

In the process of alkali-activated reaction, NaOH promotes the dissolution of fly ash particles, and Si and Al release them out into the pore solution, which contributes to the formation of zeolites [33, 34]. However, the Si/Al ratios of chabazite, faujasite, Na-P1 zeolite, and sodalite are different. Thus, the concentration of Si and Al in pore solution determines the composition and kinds of zeolites. Moreover, excessive alkali concentration also inhibits the crystallization of zeolites and results in the transformation of zeolite phases [34, 35]. Faujasite and sodalite can be regarded as the precursors of chabazite and Na-P1 zeolites which are more stable under high alkali conditions and high temperature, especially under the curing of long term [26].

Figure 6 shows the IR spectra of FABG with different sodium hydroxide contents after curing at 90°C. As seen in Figures 6(a) and 6(c), the internal vibration peak of Si-O-Si at 451 cm<sup>-1</sup> and the asymmetric vibration peak of Si (Al) -O

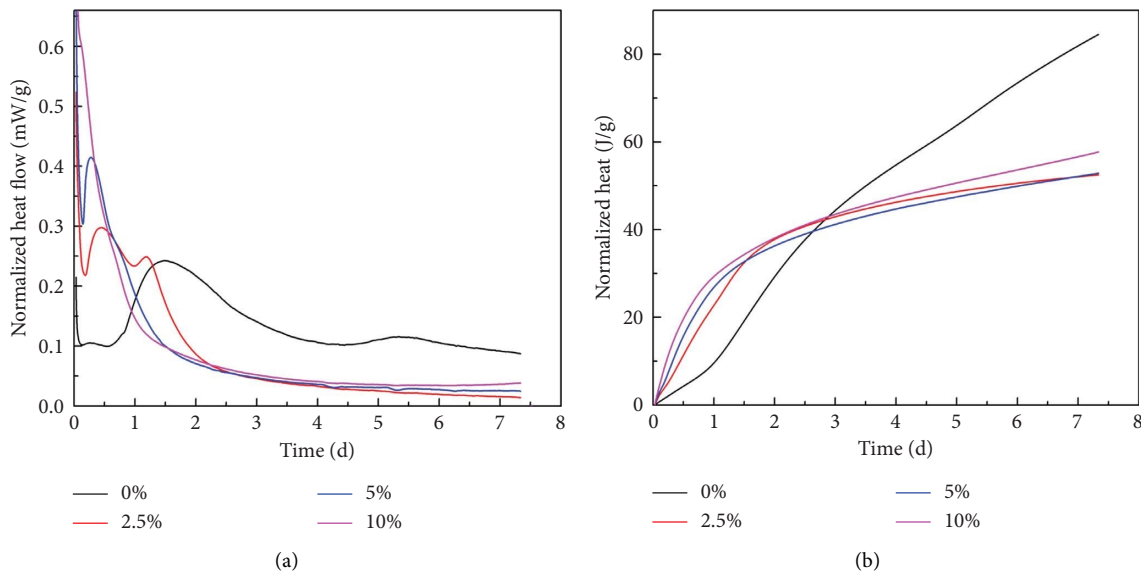


FIGURE 3: The hydration exothermic curves of FCP with different sodium hydroxide contents at 20°C: (a) normalized heat flow; (b) normalized heat.

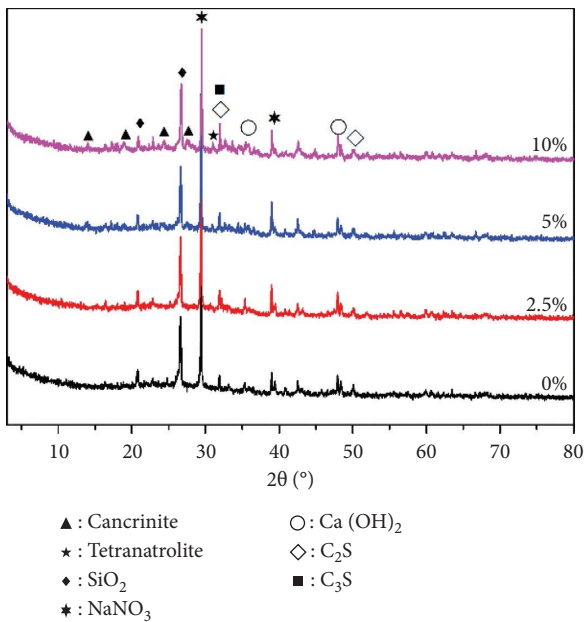


FIGURE 4: The XRD patterns of SFCM with different sodium hydroxide contents after curing at 20°C for 7 d.

at 1023 cm<sup>-1</sup> are obviously enhanced with the increase in sodium hydroxide contents at the curing age of 1 d and 28 d. This indicates that the formation of zeolites increases with the increase in sodium hydroxide contents at the curing age of 1 d and 28 d [29]. As seen in Figure 6(b), the peak intensities of two zeolite-related vibration peaks do not change significantly at the curing age of 7 d.

Figure 7 shows the SEM images of zeolites and N-A-S-H gels in FABG after curing at 90°C for 28 d. It can be seen that the main zeolite phase in geopolymers matrices is the chabazite phase, and there are a large number of N-A-S-H

gels when the sodium hydroxide content is 10%, as shown in Figures 7(a) and 7(b). When the sodium hydroxide content is 15%, there are a large number of chabazite and Na-P1 zeolites in geopolymers matrices, while N-A-S-H gels have significantly reduced, and other types of zeolites such as sodalite appear, as seen in Figures 7(c) and 7(d). When the sodium hydroxide content increases to 20%, the main zeolite phase in geopolymers matrices is Na-P1 zeolite instead of chabazite, while there are no obvious N-A-S-H gels. The internal structure becomes loose and porous, as shown in Figures 7(e) and 7(f). Figure 8 shows the SEM images of chabazite in geopolymers matrices with a sodium hydroxide content of 15%.

It can be seen that chabazite mainly synthesizes in the pores of geopolymers matrices, which is similar to the distribution of Na-P1 zeolite [27]. There is a well mass balance between [OH<sup>-</sup>] and [Na<sup>+</sup>, K<sup>+</sup>] in pore solution which provides a stable and durable condition for the crystallization of zeolites. Indeed, the pH and Na<sup>+</sup>, K<sup>+</sup> concentrations of the pore solution increase continually with the extend of curing age. [36].

As seen in Figure 9 and Table 2, the porosity of FABG increases with the increase in sodium hydroxide contents, as the introduction of sodium hydroxide promotes the formation of various zeolite phases in the matrix. Compared with the N-A-S-H gel structure, the skeleton formed by zeolite phases is looser, resulting in an increase in porosity. The average pore diameter reaches the maximum at a sodium hydroxide content of 15%, while it decreases at a sodium hydroxide content of 20%. It indicates that the large number of zeolite phases increases porosity but refines the pore size at a sodium hydroxide content of 20%, which is consistent with the results of SEM (Figure 7). In addition, the N-A-S-H gels in the matrix increase due to the strong alkali excitation effect when the sodium hydroxide content is 20%.

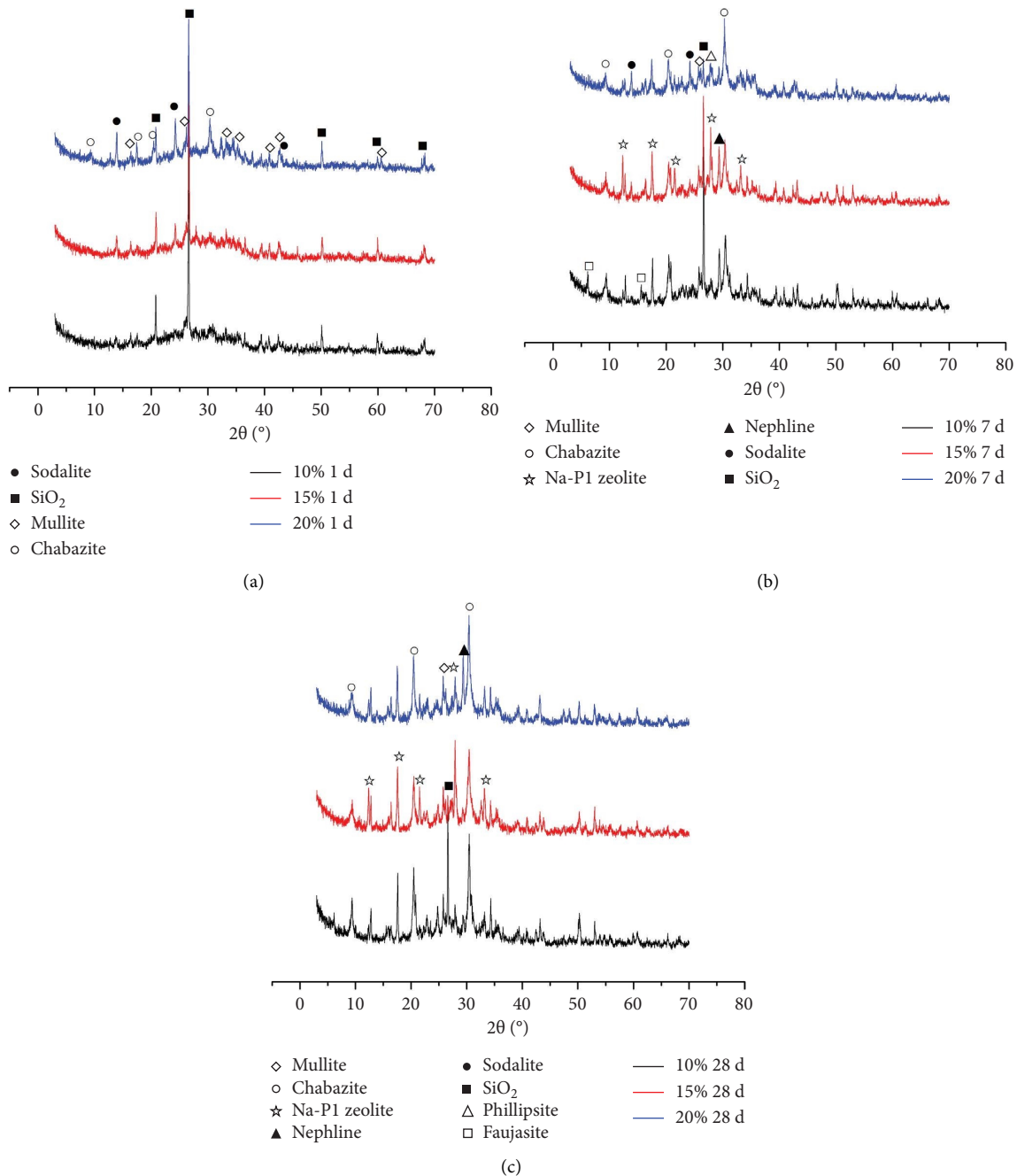


FIGURE 5: The XRD patterns of FABG with different sodium hydroxide contents after curing at 90°C: (a) 1 d; (b) 7 d; (c) 28 d.

Meanwhile, increasing N-A-S-H gels also refine the pores of geopolymer matrices.

**3.3. Products of SFCM with High Na Content.** Figure 10 shows the XRD patterns of SFCM after curing at 90°C for 28 d. As seen in Figure 10(a), Na-P1 zeolite and chabazite appear simultaneously in the SFCM when the sodium hydroxide content is above 5%. With the increase in sodium hydroxide contents, the peak intensity of SiO<sub>2</sub> in the matrix gradually decreases, which indicates that an increasing content of SiO<sub>2</sub> has been involved in the reaction. It can be

seen in Figure 10(b) that there was an obvious diffraction peak of Na-P1 zeolite at the concentration of sodium nitrate between 0 and 400 g/L. The diffraction peaks of Na-P1 zeolite decrease with the increase in sodium nitrate concentrations and disappear at 500 g/L. The diffraction peak intensity of chabazite increases with increasing sodium nitrate concentrations, but there is no obvious diffraction peak at 0 g/L and 100 g/L.

Figure 11 shows the IR curves of SFCM after curing at 90°C for 28 d. As seen in Figure 11(a), the strength of N-O bonds at a sodium hydroxide content of 5% and 10% is lower than that at 0.82%, which indicates that some sodium nitrate

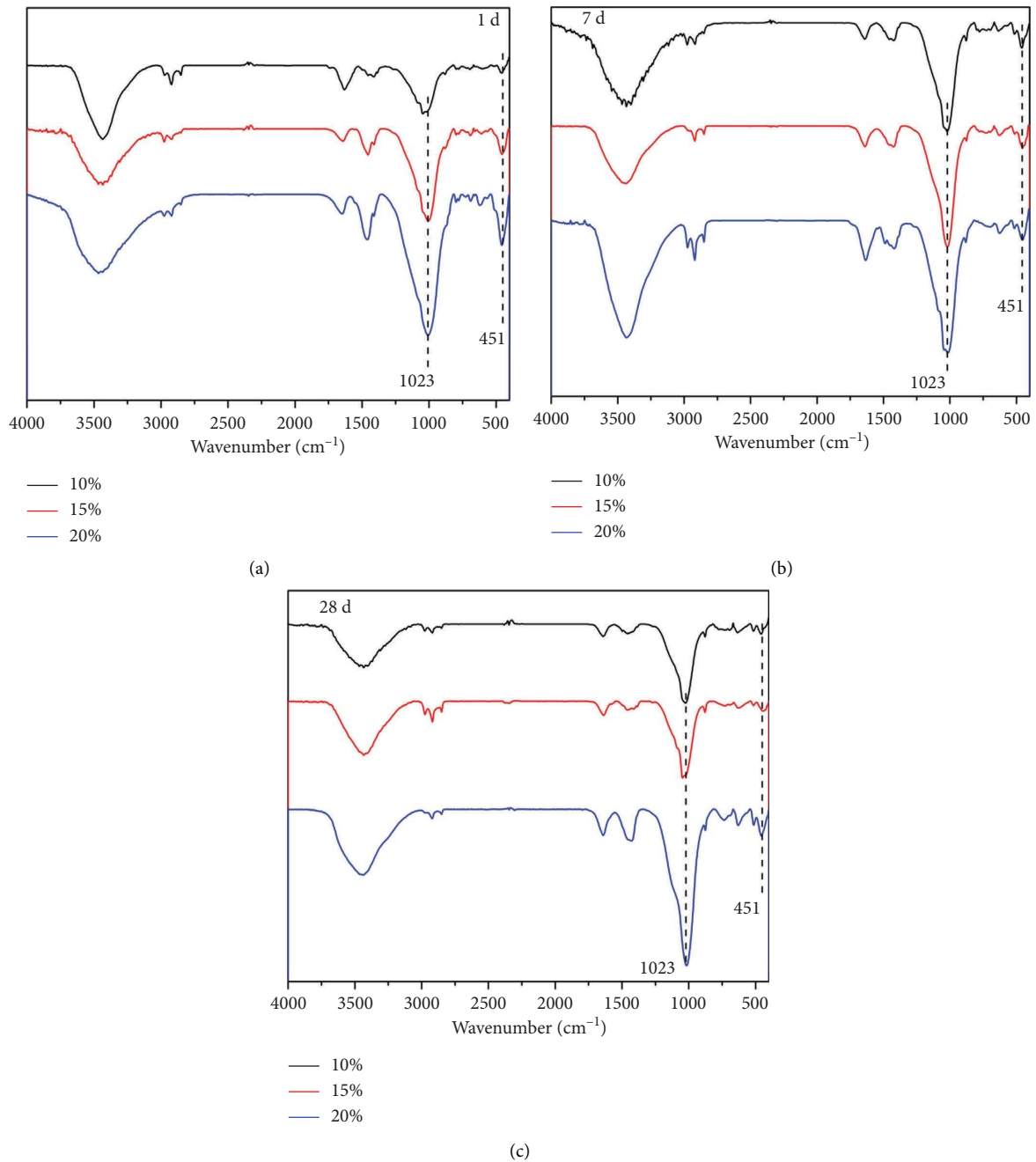


FIGURE 6: The IR spectra of FABG with different sodium hydroxide contents after curing at 90°C: (a) 1 d; (b) 7 d; (c) 28 d.

in the matrix is involved in the formation of the zeolite phase. At a wave number of  $1049\text{ cm}^{-1}$ , the strength of the Si-O-T bond [26, 29] corresponding to N-A-S-H gels and zeolite phase increases with increasing sodium hydroxide contents. As seen in Figure 11(b), the N-O bond at  $1384\text{ cm}^{-1}$  [37] increases significantly with the increase in sodium nitrate concentrations, while the Si-O-T bond corresponding to N-A-S-H gels and zeolite phase does not change significantly at a wave number of  $1045\text{ cm}^{-1}$ .

Figure 12 shows the SEM images of the SFCM with different sodium hydroxide contents after curing at 90°C for 28 d. As seen in Figure 12(a), the products of the SFCM are

still dominated by N-A-S-H gels when the sodium hydroxide content is 0.82%, while there is no obvious zeolite phase. When the sodium hydroxide content is 5%, well-crystallized chabazite appears in solidified matrices, as shown in Figure 12(b). It can be seen in Figures 12(c) and 12(d) that a large amount of chabazite appears in the SFCM when the sodium hydroxide content increases to 10%, while well-crystallized Na-P1 zeolite also appears, which is in agreement with the conclusion from XRD patterns.

Figure 13 shows the SEM images of the SFCM with different sodium nitrate concentrations after curing at 90°C for 28 d. As seen in Figure 13(a), Na-P1 zeolite is the main

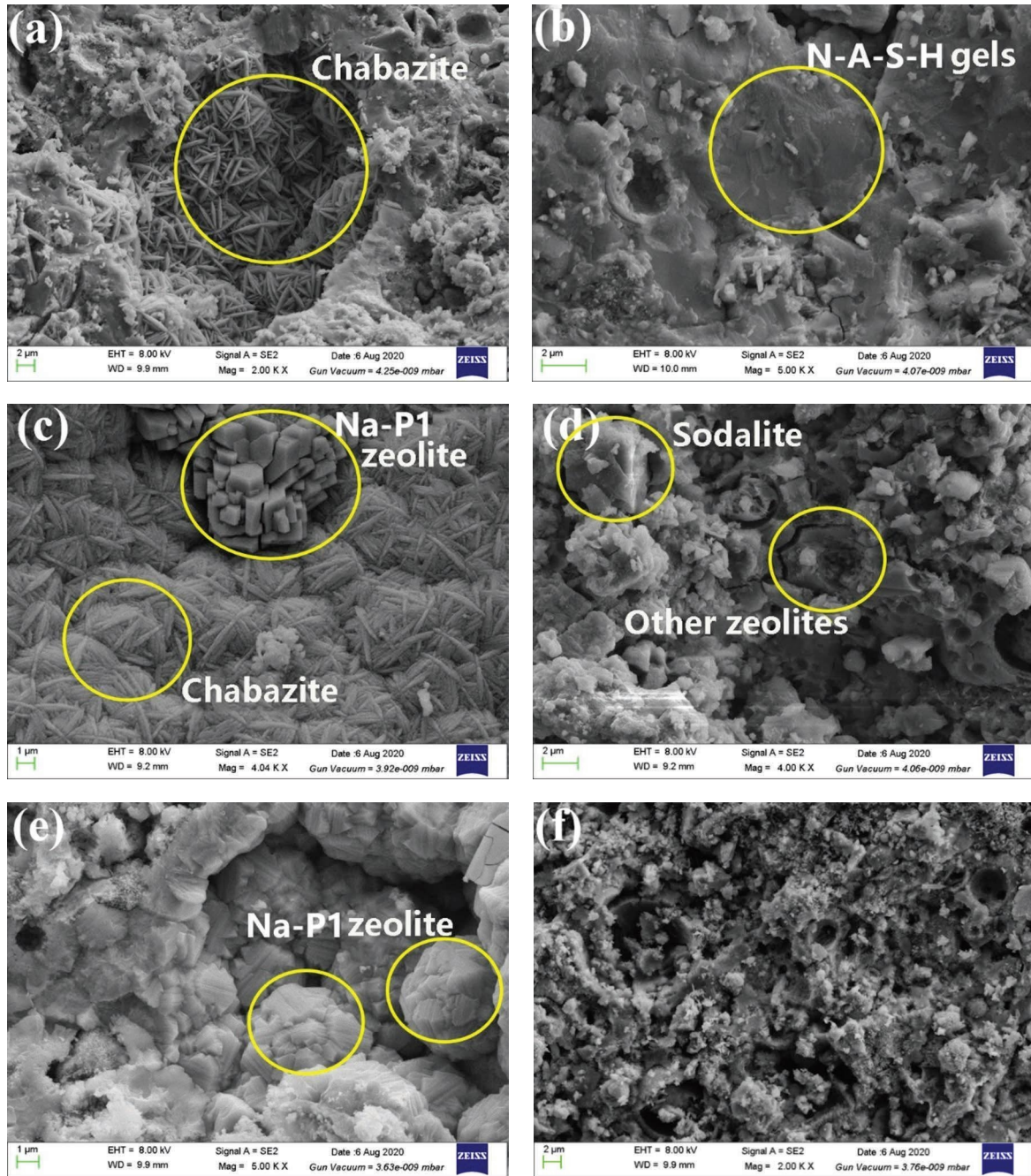


FIGURE 7: The SEM images of zeolites and N-A-S-H gels in geopolymers after curing at 90°C for 28 d. (a) and (b) Sodium hydroxide content of 10%; (c) and (d) sodium hydroxide content of 15%; (e) and (f) sodium hydroxide content of 20%.

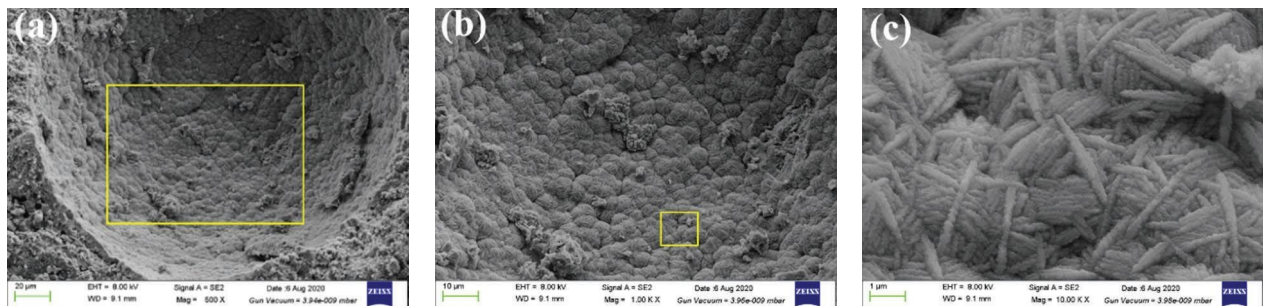


FIGURE 8: The SEM images of chabazite in geopolymers matrices with a sodium hydroxide content of 15% after curing at 90°C for 28 d.



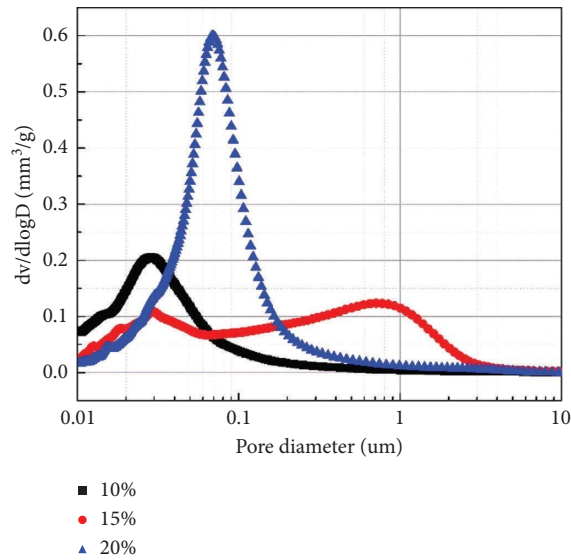


FIGURE 9: The pore size distribution of FABG with different sodium hydroxide contents after curing at 90°C for 28 d.

TABLE 2: The pore structure parameters of FABG with different sodium hydroxide contents after curing at 90°C for 28 d.

NaOH content (%)	10	15	20
Porosity (%)	24.72	31.70	40.80
Average pore size (nm)	24.20	62.24	55.14

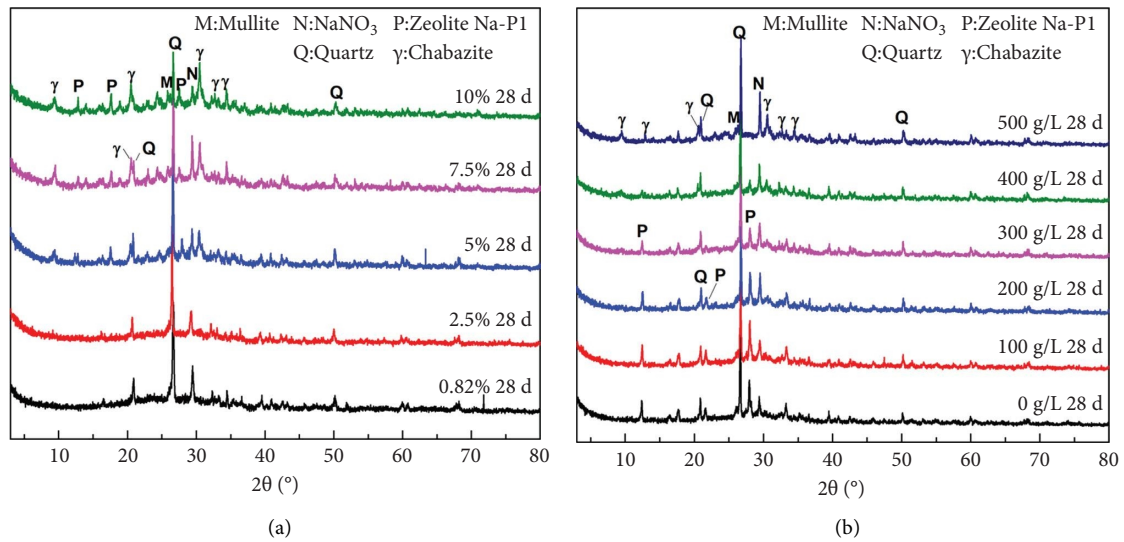


FIGURE 10: XRD patterns of the SFCM after curing at 90°C for 28 d. (a) Sodium hydroxide content; (b) sodium nitrate concentration.

phase in the SFCM when sodium nitrate concentration is 100 g/L, as shown in Figure 13(a). As seen in Figure 13(b), it can be seen that the zeolite phase in the SFCM is mainly the chabazite phase when the concentration of sodium nitrate is 500 g/L and Na-P1 zeolite is not found, which is also in agreement with the conclusion from XRD patterns.

Compared with the existence of chabazite under different alkalinity after curing at 90°C for 7 d [26], the co-existence of two zeolites (chabazite and Na-P1 zeolite)

appears in solidified matrices after 28 d. Indeed, Na-P1 zeolite just can exist at sodium nitrate concentrations below 100 g/L after curing at 90°C for 7 d, while this concentration threshold increases to 400 g/L after curing for 28 d [26]. This indicates that the extension of curing age promotes the formation and enhances the stability of Na-P1 zeolite under long-term curing.

Figure 14 and Table 3 show the pore structure distribution and pore structure parameters of the SFCM with

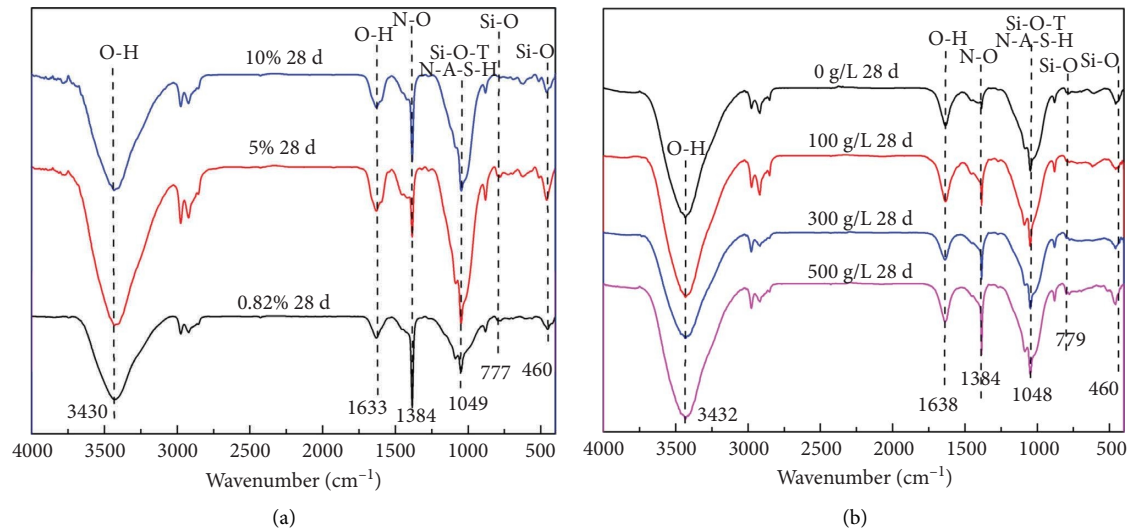


FIGURE 11: The IR curves of the SFCM after curing at 90°C for 28 d. (a) Sodium hydroxide contents; (b) sodium nitrate concentrations.

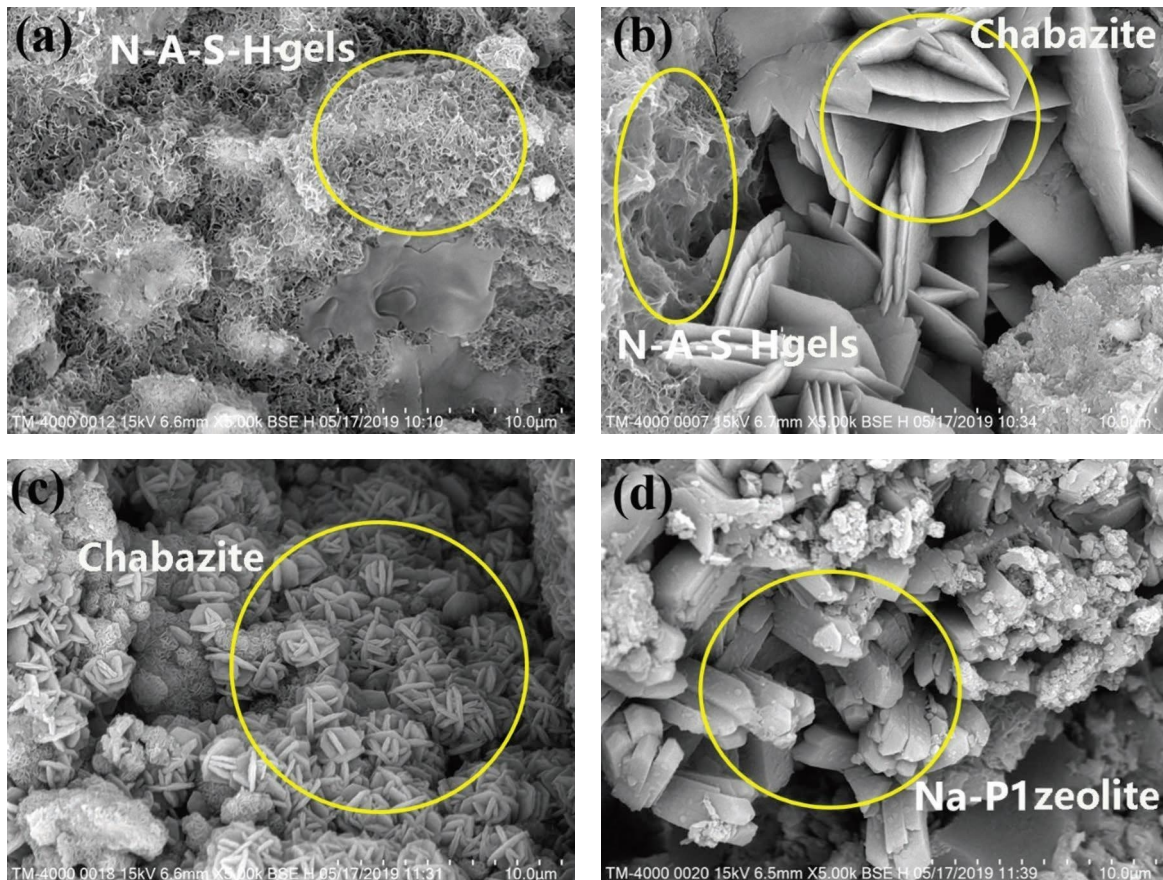


FIGURE 12: The SEM images of the SFCM with different sodium hydroxide contents after curing at 90°C for 28 d. (a) 0.82%, 300 g/L; (b) 5%, 300 g/L; (c) 10%, 300 g/L; and (d) 10%, 300 g/L.

different sodium hydroxide contents after 28 d of curing at 90°C, respectively. As seen in Figure 14(a), the peak in the curve of the pore structure shifts to the low pore size region at the sodium hydroxide content ranging from 0.82% to 2.5%, which corresponds to the decrease of the average pore

size. When the sodium hydroxide content increases to 5%, the peak in the pore size distribution curve is still below 100 nm, but the proportion of pores corresponding to 100–1000 nm increases, and the average pore size increases to 61.65 nm, as seen in Figure 14(b). The peak of the pore size

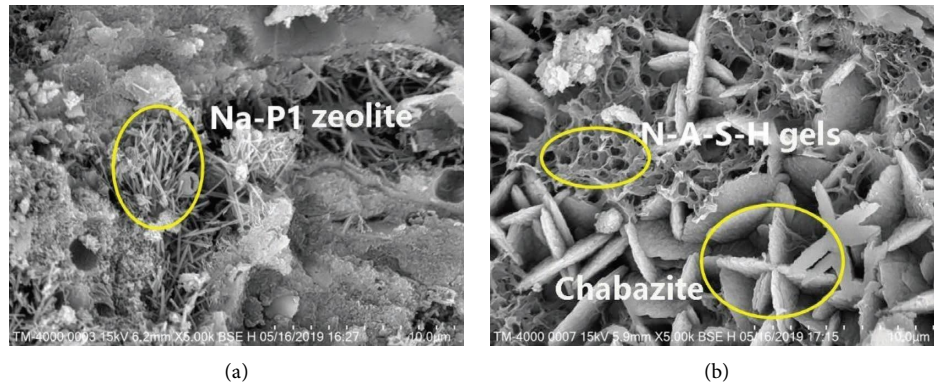


FIGURE 13: The SEM images of fly ash/cement solidified with different sodium nitrate concentrations after curing at 90°C for 28 d are shown as follows: (a) 100 g/L, 5%; (b) 500 g/L, 5%.

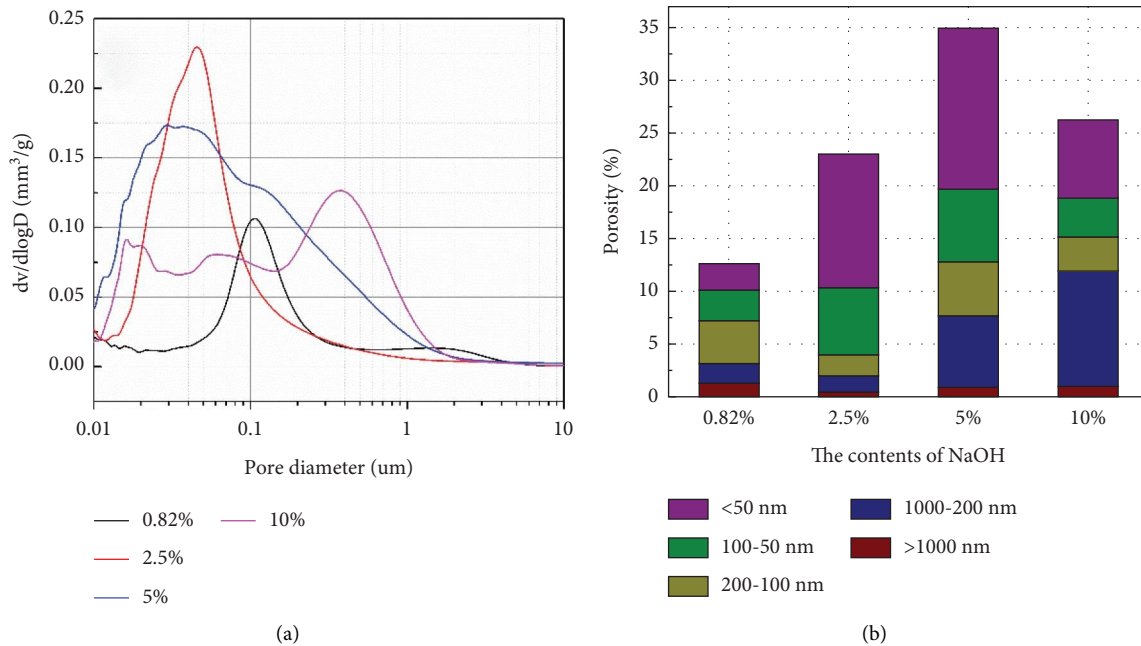


FIGURE 14: The pore structure of the SFCM with different sodium hydroxide contents after curing at 90°C for 28 d. (a) Distribution curve; (b) porosity ratio.

TABLE 3: The pore structure parameters of the SFCM with different sodium hydroxide contents after curing at 90°C for 28 d.

NaOH content (%)	0.82	2.5	5	10
Porosity (%)	12.59	23.02	34.92	26.23
Average pore size (nm)	112.6	45.62	61.65	156.7

distribution curve is about 400 nm at a sodium hydroxide content of 10%, while the average pore size increases to 156.7 nm. Moreover, the proportion of pores between 200 and 1000 nm increases significantly, as shown in Figure 14(b). Above all, the total porosity increases first and then decreases with the increase in sodium hydroxide contents. The maximum porosity is 34.92% at a sodium hydroxide content of 5% and decreases to 26.63% at a sodium hydroxide content of 10%.

Figure 15 and Table 4 show the pore structure distribution and pore structure parameters of the SFCM with different concentrations of sodium nitrate after 28 d of curing at 90°C, respectively. It can be seen in Figure 15 that the peak of the pore size distribution curve shifts to the direction of a large pore size with increasing sodium nitrate concentrations between 0 and 300 g/L, which corresponds to the increase of the average pore size. The average pore size at 300 g/L of sodium nitrate is 61.65 nm, which is 3 times that of

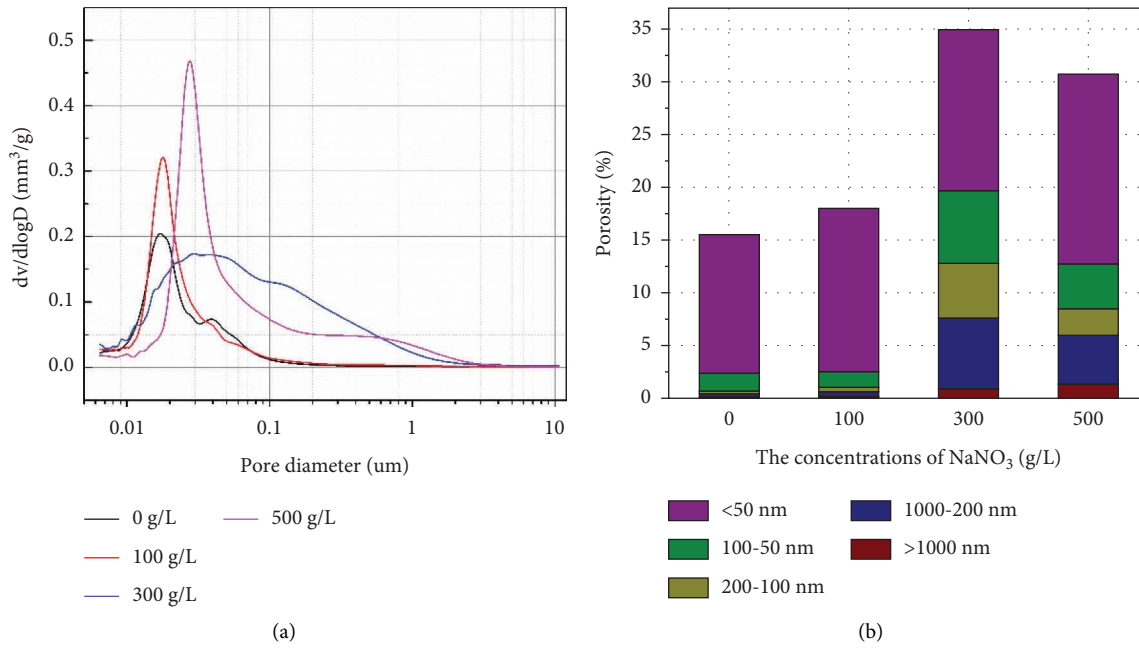


FIGURE 15: The pore structure of the SFCM with different concentrations of sodium nitrate after curing at 90°C for 28 d. (a) Distribution curve; (b) porosity ratio.

TABLE 4: The pore structure parameters of the SFCM with different concentrations of sodium nitrate after curing at 90°C for 28 d.

NaNO <sub>3</sub> concentration (g/L)	0	100	300	500
Porosity (%)	15.54	18.05	34.92	30.75
Average pore size (nm)	20.36	20.06	61.65	38.05

0 g/L of sodium nitrate. The peak shape of the pore size distribution curve becomes wider, and the porosity of regions above 50 nm increases greatly. When the concentration of sodium nitrate is 500 g/L, the peak value of the pore size distribution curve is not significantly different from that at 300 g/L, but the peak shape becomes narrow and porosity begins to decrease, and the average pore size also decreases to 38.05 nm. Moreover, the proportion of pores below 50 nm and above 1000 nm increases, and the proportion of pores between 50 nm and 1000 nm decreases significantly.

Following the increase of sodium hydroxide and sodium nitrate, porosity shows an increasing trend due to the big interval between zeolites. However, compared with the pore structure of the SFCM after curing for 7 d [26], the porosity of the SFCM after curing for 28 d significantly reduces, which is mainly attributed to further deepened alkali activation reaction and the presence of a large number of zeolites and N-A-S-H gels that fill larger pores in the SFCM [27].

**3.4. Leaching Characteristics of SFCM.** Figure 16 shows the leaching curves of  $\text{Ca}^{2+}$  in the SFCM containing different concentrations of sodium nitrate at a sodium hydroxide content of 5%. As seen in Figure 16(a), the LF of  $\text{Ca}^{2+}$  in the SFCM increases with the increase in sodium nitrate concentrations. Figure 16(b) shows that the CLF of  $\text{Ca}^{2+}$  in the

SFCM also increases significantly with increasing sodium nitrate concentrations, among which the increase is more obvious at concentrations of 400 and 500 g/L. When the leaching period is prolonged to 90 d, the CLF of  $\text{Ca}^{2+}$  is about 0.11 cm at a concentration of 400–500 g/L, while it is about 0.09 cm at a concentration of 100–300 g/L. Moreover, the CLF of  $\text{Ca}^{2+}$  is only about 0.07 cm at a sodium nitrate concentration of 0 g/L.

Figure 17 displays the leaching curves of  $\text{Ca}^{2+}$  in the SFCM with different sodium hydroxide contents at a sodium nitrate concentration of 300 g/L. As seen in Figure 17(a), the LF of  $\text{Ca}^{2+}$  in the SFCM increases with the increase in sodium hydroxide contents. Figure 17(b) shows that the CLF of  $\text{Ca}^{2+}$  in the SFCM also increases with increasing sodium hydroxide contents. Moreover, at the leaching period of 28 d, the CLF of  $\text{Ca}^{2+}$  has no obvious change when sodium hydroxide contents range from 0.82% to 5%, which is about 0.07 cm. When the sodium hydroxide content is 7.5% and 10%, the CLF of  $\text{Ca}^{2+}$  increases obviously, about 0.10 cm. It can be found that sodium hydroxide inhibits the decalcification of the SCM [32] but promotes the decalcification of the SFCM.

Figure 18 exhibits the leaching curves of  $\text{Sr}^{2+}$  in the SFCM containing different concentrations of sodium nitrate at a sodium hydroxide content of 5%. Figures 18(a) and 18(b) show that the LF and CLF of  $\text{Sr}^{2+}$  in the SFCM at 300 g/L are lower than those of pure water. However, the LF and

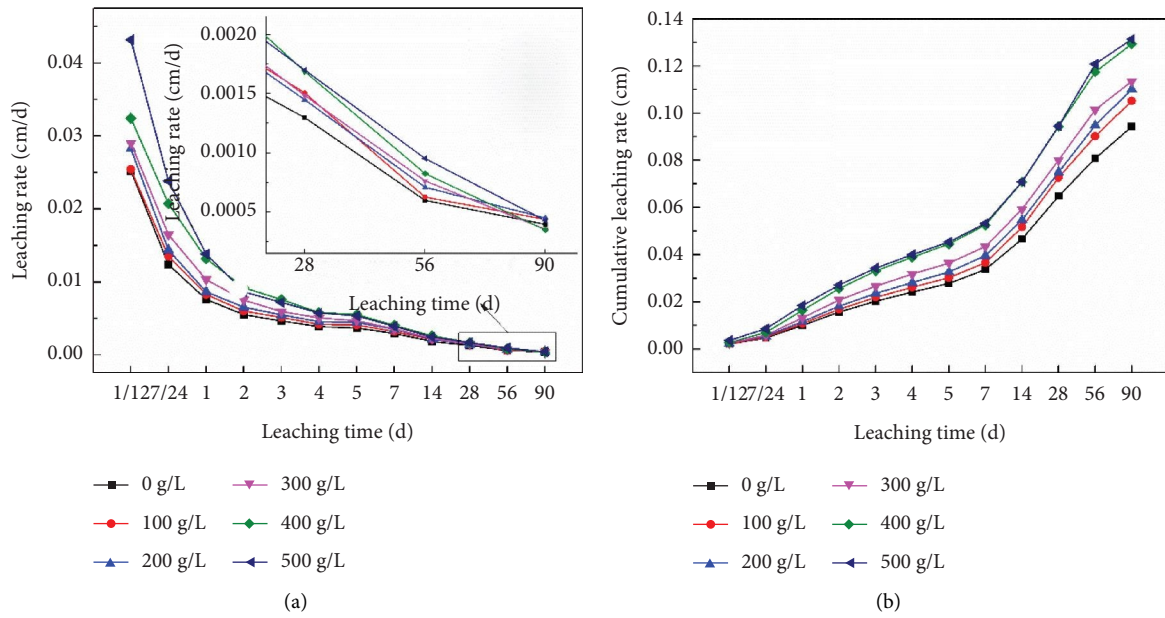


FIGURE 16: The leaching curves of Ca<sup>2+</sup> in the SFCM with different concentrations of sodium nitrate at a sodium hydroxide content of 5%: (a) LF of Ca<sup>2+</sup>; (b) CLF of Ca<sup>2+</sup>.

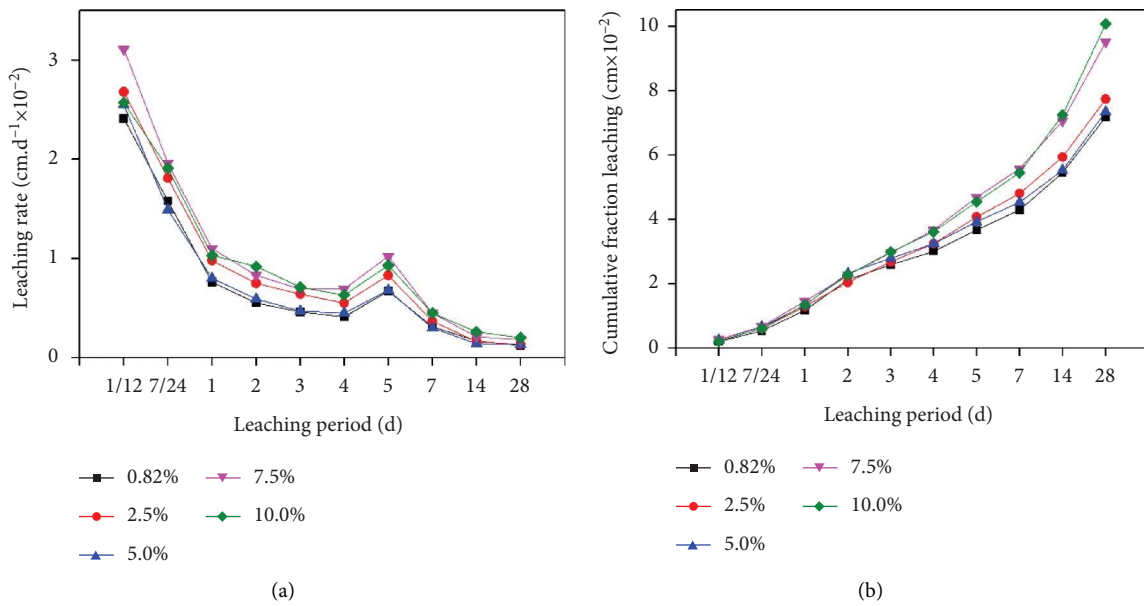


FIGURE 17: The leaching curves of Ca<sup>2+</sup> in the SFCM with different sodium hydroxide contents at a sodium nitrate concentration of 300 g/L: (a) LF of Ca<sup>2+</sup>; (b) CLF of Ca<sup>2+</sup>.

CLF of other sodium nitrate concentrations are higher than those of pure water, and the highest value is at a sodium nitrate concentration of 100 g/L.

Figure 19 shows the leaching curves of Sr<sup>2+</sup> in the SFCM with different sodium hydroxide contents at a sodium nitrate concentration of 300 g/L. As seen in Figure 19(a), it can be found that the LF of Sr<sup>2+</sup> in the SFCM decreases first and then increases with the increase in sodium hydroxide contents. Besides, the lowest value is obtained at a sodium hydroxide content of 5%. As seen in Figure 19(b), the CLF of

Sr<sup>2+</sup> in the SFCM also decreases first and then increases with the increase in sodium hydroxide contents. Indeed, the variation amplitude increases with the increase in the leaching period. When the leaching period reaches 28 d, the CLF of Sr<sup>2+</sup> obtains the maximum of 0.12 cm at a sodium hydroxide content of 0.82%; when the content of sodium hydroxide is 5%, the CLF of Sr<sup>2+</sup> is the lowest, only about 0.04 cm. When the sodium hydroxide content increases to 10%, the CLF of Sr<sup>2+</sup> begins to rise again, reaching about 0.06 cm. Although the conversion of N-A-S-H gels to the

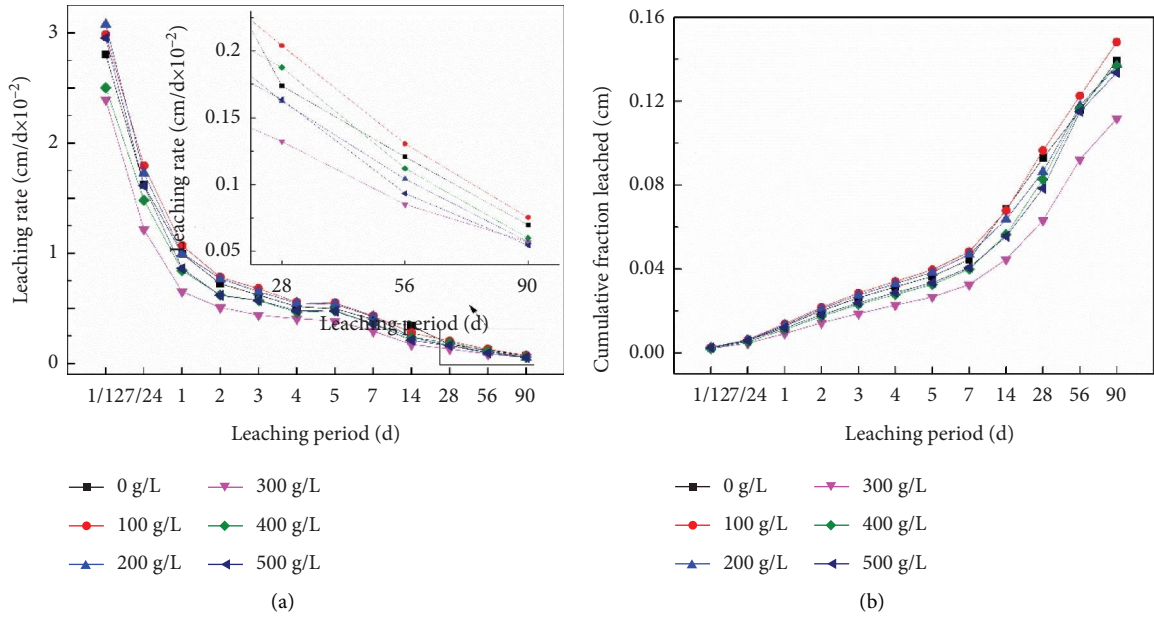


FIGURE 18: The leaching curves of  $Sr^{2+}$  in the SFCM containing different concentrations of sodium nitrate at a sodium hydroxide content of 5%: (a) LF; (b) CLF.

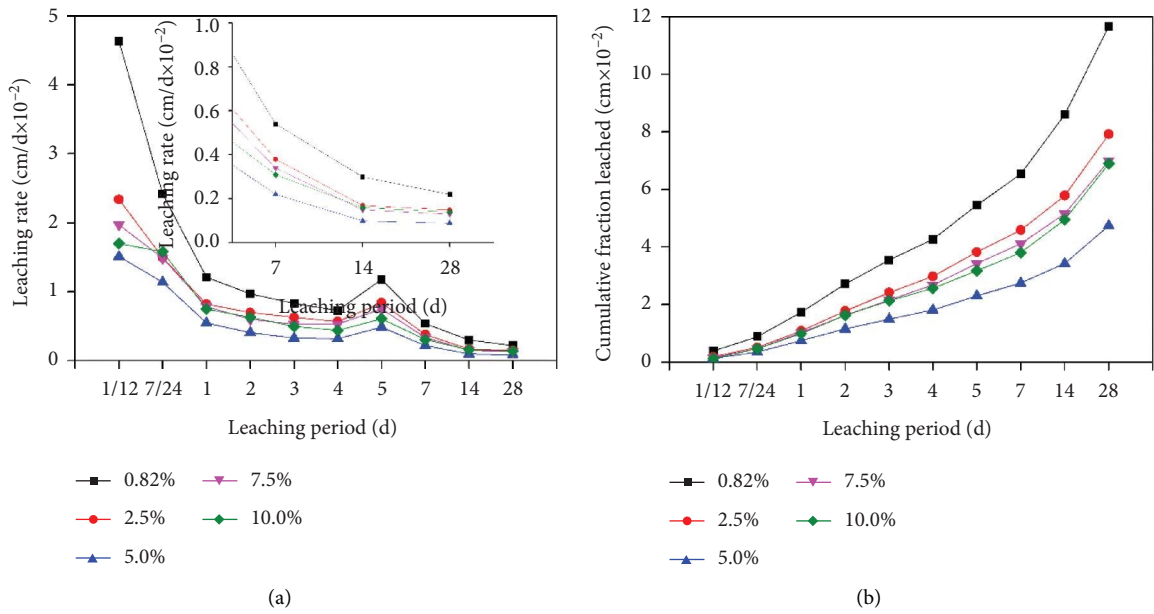


FIGURE 19: The leaching curves of  $Sr^{2+}$  in the SFCM with different sodium hydroxide contents at a sodium nitrate concentration of 300 g/L: (a) LF; (b) CLF.

zeolite phase can improve the retention capacity of the SFCM for simulated radionuclides [38–42], the porosity and the average pore size of the SFCM increase with the formation of a large number of zeolites, which will result in an increase in the LF of  $Sr^{2+}$  [26, 28]. Just a proper number of zeolites can effectively inhibit the leaching of radionuclides  $Sr^{2+}$ .

Figure 20 displays the leaching curves of  $Cs^+$  in the SFCM containing different concentrations of sodium nitrate after curing for 28 d at a sodium hydroxide content of 5%. It

can be seen in Figure 20(a) that the LF of  $Cs^+$  in the SFCM decreases significantly with the increase in sodium nitrate concentrations at each leaching period. As seen in Figure 20(b), the CLF of  $Cs^+$  in the SFCM decreases significantly with the increase in sodium nitrate concentrations, but the degree of the decrease increases with the increase in the leaching period. When the leaching period is 90 d, the CLF of  $Cs^+$  in the SFCM is about 0.14 cm when sodium nitrate is not added, while the CLF of  $Cs^+$  in the SFCM with 500 g/L of sodium nitrate is only about 0.10 cm.

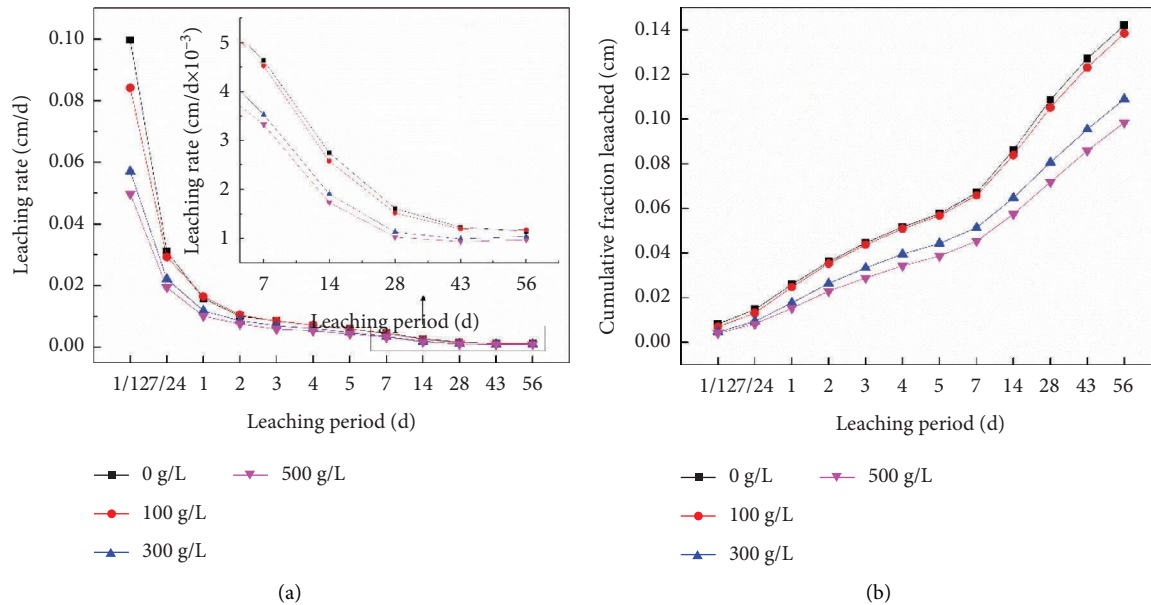


FIGURE 20: The leaching curves of Cs<sup>+</sup> in the SFCM containing different concentrations of sodium nitrate at a sodium hydroxide content of 5%: (a) LF; (b) CLF.

Figure 21 displays the leaching curves of Cs<sup>+</sup> in the SFCM with different sodium hydroxide contents after curing for 28 d at a sodium nitrate concentration of 300 g/L. As seen in Figure 21(a), the LF of Cs<sup>+</sup> in the SFCM increases first and then decreases with the increase in sodium hydroxide contents. Figure 21(b) shows that the CLF of Cs<sup>+</sup> in the SFCM also increases first and then decreases with the increase in sodium hydroxide contents. With the increase in the leaching period, the variation of the CLF of Cs<sup>+</sup> becomes greater. When the leaching period is 90 d, the CLF of Cs<sup>+</sup> obtains the lowest value of ~0.05 cm at a sodium hydroxide content of 0.82% while it reaches the highest value of ~0.11 cm at a sodium hydroxide content of 5%. The CLF of Cs<sup>+</sup> at a sodium hydroxide content of 10% is lower than that of 5%, which is about 0.09 cm.

This study examines the FABG and SFCM for the immobilization of Sr<sup>2+</sup> and Cs<sup>+</sup>. The SFCM possesses both the advantage of geopolymer and cement in the adsorption of radionuclides [1, 43]. Moreover, the curing time is an important factor that influences the end product type. Comparing the results under the curing time of 7 d [26], the conclusions obtained at 28 d are much different.

Above all, sodium nitrate and sodium hydroxide both accelerate the decalcification of the SFCM, which increases the degradation of matrices and results in further leaching of radionuclides. Though sodium nitrate promotes the leaching of Sr<sup>2+</sup>, sodium hydroxide inhibits leaching effectively. As Sr<sup>2+</sup> is always adsorbed or incorporated in hydration products of cement, the leaching of Sr<sup>2+</sup> is mainly determined by the transformation of C-S-H and ettringite under different conditions of sodium salts. Sodium nitrate decreases, while sodium hydroxide increases nonbridging oxygen, which results in the change of Sr<sup>2+</sup> leaching [28, 32].

However, the effect of sodium salts on the leaching of Cs<sup>+</sup> is opposite. The LF and CLF of Cs<sup>+</sup> decrease with the increase in sodium nitrate concentrations after curing for 28 d. Moreover, the change in the pore structure of the SFCM after curing for 28 d is due to the increase in the zeolite content and the decrease in the gels phase in the SFCM with the extension of curing time. Indeed, excessive zeolite causes the loose and porous internal structure of the SFCM. However, increasing chabazite with high adsorption of Cs<sup>+</sup> can neutralize the negative effect of pore structures, which leads to the prevention of Cs<sup>+</sup> leaching [23, 24]. However, the LF and CLF of Cs<sup>+</sup> in the presence of high sodium hydroxide content are higher than those of low sodium hydroxide content (0.82%), which is mainly due to the increase in the porosity and average pore size of the SFCM (Figure 14). At the same time, the coexistence of chabazite and Na-P1 zeolite occurs at the sodium hydroxide content above 5%. The adsorption capacity of Na-P1 zeolite for Cs<sup>+</sup> is weaker than that of chabazite but stronger than that of N-A-S-H gels [23, 24, 44, 45], which results in the reduction of Cs leaching at a sodium hydroxide content of 10% compared to 5% and 2.5%.

The cumulative leaching fractions of Sr<sup>2+</sup> and Cs<sup>+</sup> in SFCM of this study are both below 0.05 cm at the leaching period of 28 d, which is much lower than that of the pure cement matrices or geopolymer matrices in other researches [43, 46–48]. Especially, the technology of in situ synthesis of zeolites promotes the immobilization of radionuclides substantially despite the increasing porosity. However, the SFCM is hard to reach an excellent immobilization performance for Sr<sup>2+</sup> and Cs<sup>+</sup> at the same time. So, further research on the composition of the SFCM and curing regime is needed.

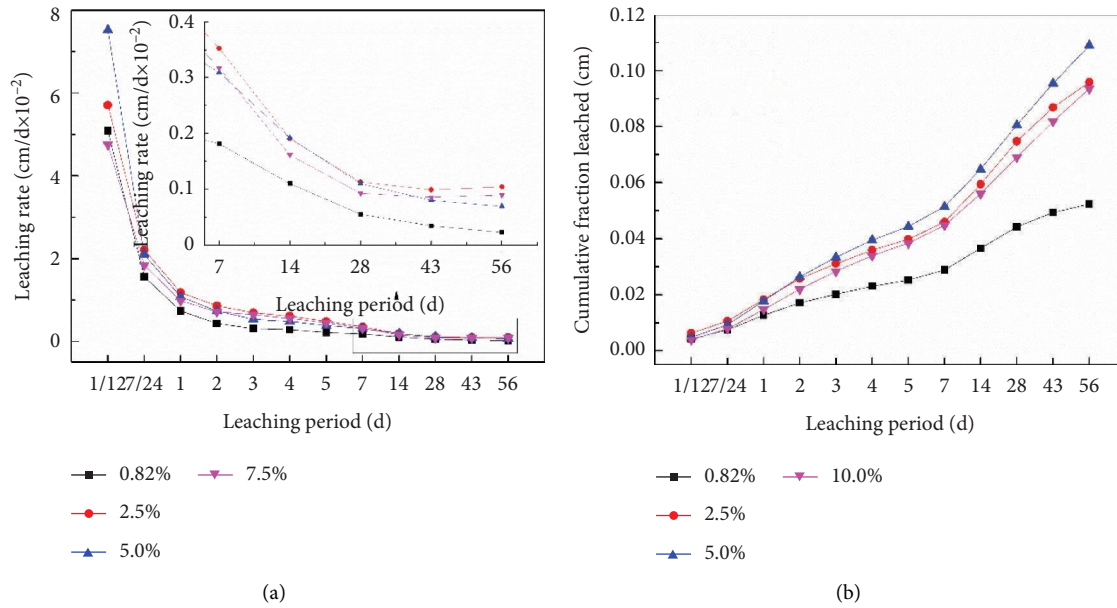


FIGURE 21: The leaching curves of Cs<sup>+</sup> in the SFCM with different sodium hydroxide contents at a sodium nitrate concentration of 300 g/L: (a) LF; (b) CLF.

#### 4. Conclusions

Though the introduction of fly ash delayed the reaction and reduced the hydration heat of the SFCM, fly ash-based geopolymers at room temperature have no obvious crystalline phase except a little amount of cancrinite and tetranatrolite at high sodium hydroxide content. However, FABG preferred to transform into ordered structures at a high temperature of 90°C, such as Na-P1 zeolite and chabazite. Under the excitation of sodium hydroxide, the main zeolite phases generated at different sodium hydroxide contents (10%, 15%, and 20%) were chabazite and Na-P1 zeolite. Zeolites are easy to crystallize in pores under the conditions of enough alkali. In the SFCM, the sodium hydroxide content required for the crystallization of Na-P1 zeolite is at least 5%. With the increase in sodium hydroxide contents, more sodium nitrate participated in the reaction to form the zeolite phase. When the sodium hydroxide content was fixed at 5% and the curing time was 28 d, the coexistence of chabazite and Na-P1 zeolite appeared under the condition of high sodium hydroxide content of more than 5%. At the same time, Na-P1 zeolite can exist at sodium nitrate concentrations below 400 g/L, while it completely transformed into the chabazite phase at 500 g/L. The addition of sodium hydroxide and sodium nitrate made the pore structure of the SFCM looser, but the opposite effect occurred when the sodium hydroxide content reached 10%. With the increase in sodium nitrate concentrations, the CLF of Ca<sup>2+</sup> increased significantly within a leaching period of 1–7 d, while the addition of high content sodium hydroxide reduced the CLF of Ca<sup>2+</sup>. The SFCM at a sodium hydroxide content of 5% or at a sodium nitrate concentration of 300 g/L obtained the lowest CLF of Sr<sup>2+</sup>. Sodium hydroxide increased the CLF of Cs<sup>+</sup>, but the CLF of Cs<sup>+</sup> decreased significantly with the increase in sodium nitrate. Comparing the kinds of zeolites

and the leaching behavior of radionuclides, it can be concluded that chabazite has a higher retention capacity for Cs<sup>+</sup>, while Na-P1 zeolite has a higher retention capacity for Sr<sup>2+</sup> [5].

#### Data Availability

The data that support the findings of this study are available from the corresponding author upon reasonable request.

#### Ethical Approval

Ethical approval is not required for this study.

#### Consent

Consent is not applicable to this study.

#### Conflicts of Interest

The authors declare no conflicts of interest.

#### Authors' Contributions

Zhao Zheng designed the methodology, conducted formal analysis and investigation, and wrote the original draft. Zhitao Bao collected resources, conducted formal analysis, and wrote and reviewed and edited the manuscript. Qingyi Wang validated the data and collected resources. Yuxiang Li conceptualized the design, collected resources, and supervised the study.

#### Acknowledgments

This work was supported by the Scientific Research Fund of the Southwest University of Science and Technology (No.



21zx7124). The authors gratefully acknowledge the School of Civil Engineering and Architecture and the School of Materials Science and Engineering (Southwest University of Science and Technology) for providing facilities to carry out the work.

## References

- [1] Y. Zhu, Z. Zheng, Y. Deng, C. Shi, and Z. Zhang, "Advances in immobilization of radionuclide wastes by alkali activated cement and related materials," *Cement and Concrete Composites*, vol. 126, Article ID 104377, 2022.
- [2] W. E. Lee, M. I. Ojovan, and C. M. Jantzen, *Radioactive Waste Management and Contaminated Site Clean-Up: Processes, Technologies and International Experience*, Elsevier, Amsterdam, Netherlands, 2013.
- [3] N. Sami, O. A. Moamen, M. El-Dessouky, and A. El-Kamash, "Assessment the leaching characteristics and long-term leaching behavior of some radionuclides from synthesized zeolite cement matrix," *Cement and Concrete Research*, vol. 143, Article ID 106357, 2021.
- [4] M. Alexander, A. Bertron, and N. D. Belie, *Performance of Cement-Based Materials in Aggressive Aqueous Environments*, Springer, Berlin, Germany, 2013.
- [5] T. Bakharev, "Resistance of geopolymer materials to acid attack," *Cement and Concrete Research*, vol. 35, no. 4, pp. 658–670, 2005.
- [6] P. Rožek, M. Król, and W. Mozgawa, "Geopolymer-zeolite composites: a review," *Journal of Cleaner Production*, vol. 230, pp. 557–579, 2019.
- [7] C. Chlique, D. Lambertin, P. Antonucci, F. Frizon, and P. Deniard, "XRD analysis of the role of cesium in sodium-based geopolymer," *Journal of the American Ceramic Society*, vol. 98, no. 4, pp. 1308–1313, 2015.
- [8] J. Melar, G. Renaudin, F. Leroux et al., "The porous network and its interface inside geopolymers as a function of alkali cation and aging," *Journal of Physical Chemistry C*, vol. 119, no. 31, pp. 17619–17632, 2015.
- [9] M. Komljenović, G. Tanasijević, N. Džunuzović, and J. L. Provis, "Immobilization of cesium with alkali-activated blast furnace slag," *Journal of Hazardous Materials*, vol. 388, Article ID 121765, 2020.
- [10] M. G. Blackford, J. V. Hanna, K. J. Pike, E. R. Vance, and D. S. Perera, "Transmission electron microscopy and nuclear magnetic resonance studies of geopolymers for radioactive waste immobilization," *Journal of the American Ceramic Society*, vol. 90, no. 4, pp. 1193–1199, 2007.
- [11] N. K. Lee, H. R. Khalid, and H. K. Lee, "Adsorption characteristics of cesium onto mesoporous geopolymers containing nano-crystalline zeolites," *Microporous and Mesoporous Materials*, vol. 242, pp. 238–244, 2017.
- [12] J. G. Jang, S. M. Park, and H. K. Lee, "Physical barrier effect of geopolymeric waste form on diffusivity of cesium and strontium," *Journal of Hazardous Materials*, vol. 318, pp. 339–346, 2016.
- [13] Q. Li, Z. Sun, D. Tao et al., "Immobilization of simulated radionuclide  $^{133}\text{Cs}^+$  by fly ash-based geopolymer," *Journal of Hazardous Materials*, vol. 262, pp. 325–331, 2013.
- [14] S. Petlitckaia, Y. Barré, T. Pierrat, O. Grauby, D. Ferry, and A. Poulesquen, "Functionalized geopolymer foams for cesium removal from liquid nuclear waste," *Journal of Cleaner Production*, vol. 269, Article ID 122400, 2020.
- [15] Q. Tian and K. Sasaki, "A novel composite of layered double hydroxide/geopolymer for co-immobilization of  $\text{Cs}^+$  and  $\text{SeO}_4^{2-}$  from aqueous solution," *Science of the Total Environment*, vol. 695, Article ID 133799, 2019.
- [16] J. Luo, W. Zhang, H. Yang et al., "Halide perovskite composites for photocatalysis: a mini review," *EcoMat*, vol. 3, no. 1, 2021.
- [17] Z. Zhang, X. Ding, X. Yang, W. Tu, L. Wang, and Z. Zou, "Shedding light on  $\text{CO}_2$ : catalytic synthesis of solar methanol," *EcoMat*, vol. 3, no. 1, 2021.
- [18] E. A. Dobretsova, X. Xia, A. Pant et al., "Hydrothermal synthesis of  $\text{Yb}^{3+}$ :  $\text{LuLiF}_4$  microcrystals and laser refrigeration of  $\text{Yb}^{3+}$ :  $\text{LuLiF}_4$ /silicon-nitride composite Nanostructures," *Laser & Photonics Reviews*, vol. 15, no. 10, Article ID 2100019, 2021.
- [19] Q. Mo, C. Chen, W. Cai, S. Zhao, D. Yan, and Z. Zang, "Room temperature synthesis of stable zirconia-coated  $\text{CsPbBr}_3$  nanocrystals for white light-emitting diodes and visible light communication," *Laser & Photonics Reviews*, vol. 15, no. 10, Article ID 2100278, 2021.
- [20] P. Talianov, L. I. Fatkhutdinova, A. S. Timin, V. A. Milichko, and M. V. Zyuzin, "Adaptive nanoparticle-polymer complexes as optical elements: design and application in nanophotonics and nanomedicine," *Laser & Photonics Reviews*, vol. 15, no. 9, Article ID 2000421, 2021.
- [21] L. Yuan, Y. Jin, Y. Su, H. Wu, Y. Hu, and S. Yang, "Optically stimulated luminescence materials: optically stimulated luminescence phosphors: principles, applications, and prospects (laser photonics rev. 14(12)/2020)," *Laser & Photonics Reviews*, vol. 14, no. 12, Article ID 2070068, 2020.
- [22] J. M. Newsam, "The zeolite cage structure," *Science*, vol. 231, no. 4742, pp. 1093–1099, 1986.
- [23] W. Baek, S. Ha, S. Hong, S. Kim, and Y. Kim, "Cation exchange of cesium and cation selectivity of natural zeolites: chabazite, stilbite, and heulandite," *Microporous and Mesoporous Materials*, vol. 264, pp. 159–166, 2018.
- [24] H. Aono, Y. Takeuchi, Y. Itagaki, and E. Johan, "Synthesis of chabazite and merlinoite for  $\text{Cs}^+$  adsorption and immobilization properties by heat-treatment," *Solid State Sciences*, vol. 100, Article ID 106094, 2020.
- [25] M. Munthali, E. Johan, H. Aono, and N. Matsue, " $\text{Cs}^+$  and  $\text{Sr}^{2+}$  adsorption selectivity of zeolites in relation to radioactive decontamination," *Journal of Asian Ceramic Societies*, vol. 3, no. 3, pp. 245–250, 2015.
- [26] Z. Zheng, Y. Li, H. Sun, Z. Zhang, and X. Ma, "Coupling effect of  $\text{NaOH}$  and  $\text{NaNO}_3$  on the solidified fly ash-cement matrices containing  $\text{Cs}^+$ : reaction products, microstructure and leachability," *Journal of Nuclear Materials*, vol. 539, Article ID 152252, 2020a.
- [27] Z. Zheng, X. Ma, Z. Zhang, and Y. Li, "In-situ transition of amorphous gels to Na-P1 zeolite in geopolymer: mechanical and adsorption properties," *Construction and Building Materials*, vol. 202, pp. 851–860, 2019.
- [28] Z. Zheng, Y. Li, Z. Zhang, and X. Ma, "The impacts of sodium nitrate on hydration and microstructure of Portland cement and the leaching behavior of  $\text{Sr}^{2+}$ ," *Journal of Hazardous Materials*, vol. 388, Article ID 121805, 2020b.
- [29] Z. Zheng, Y. Li, J. Yang, M. Cui, H. Wang, and X. Ma, "Insights into the deterioration of CSH gels in hardened cement pastes with different  $\text{NaNO}_3$  concentrations," *Construction and Building Materials*, vol. 259, Article ID 120423, 2020c.
- [30] A. Kumar, G. Sant, C. Patapy, C. Gianocca, and K. L. Scrivener, "The influence of sodium and potassium hydroxide on alite hydration: experiments and simulations,"

- Cement and Concrete Research*, vol. 42, no. 11, pp. 1513–1523, 2012.
- [31] B. Mota, T. Matschei, and K. Scrivener, “The influence of sodium salts and gypsum on alite hydration,” *Cement and Concrete Research*, vol. 75, pp. 53–65, 2015.
- [32] Z. Zheng, Y. Li, M. Cui et al., “Insights into the effect of NaOH on the hydration products of solidified cement- $\text{NaNO}_3$  matrices and leaching behavior of  $\text{Sr}^{2+}$ ,” *Science of the Total Environment*, vol. 755, Article ID 142581, 2021.
- [33] M. Inada, Y. Eguchi, N. Enomoto, and J. Hojo, “Synthesis of zeolite from coal fly ashes with different silica-alumina composition,” *Fuel*, vol. 84, no. 2-3, pp. 299–304, 2005.
- [34] N. Murayama, H. Yamamoto, and J. Shibata, “Mechanism of zeolite synthesis from coal fly ash by alkali hydrothermal reaction,” *International Journal of Mineral Processing*, vol. 64, pp. 1–17, 2002.
- [35] A. M. Cardoso, A. Paprocki, L. S. Ferret, C. M. Azevedo, and M. Pires, “Synthesis of zeolite Na-P1 under mild conditions using Brazilian coal fly ash and its application in wastewater treatment,” *Fuel*, vol. 139, pp. 59–67, 2015.
- [36] J. K. Tishmack, J. Olek, S. Diamond, and S. Sahu, “Characterization of pore solutions expressed from high-calcium fly-ash-water pastes,” *Fuel*, vol. 80, no. 6, pp. 815–819, 2001.
- [37] J. C. Buhl and J. Lons, “Synthesis and crystal structure of nitrate enclathrated sodalite  $\text{Na}_8[\text{AlSiO}_4](6)(\text{NO}_3)(2)$ ,” *Journal of Alloys and Compounds*, vol. 235, no. 1, pp. 41–47, 1996.
- [38] S. Bagosi and L. Csetenyi, “Caesium immobilisation in hydrated calcium-silicatealuminate systems,” *Cement and Concrete Research*, vol. 28, no. 12, pp. 1753–1759, 1998.
- [39] M. Mahima Kumar, K. Irshad, and H. Jena, “Removal of  $\text{Cs}^+$  and  $\text{Sr}^{2+}$  ions from simulated radioactive waste solutions using Zeolite-A synthesized from kaolin and their structural stability at high pressures,” *Microporous and Mesoporous Materials*, vol. 312, Article ID 110773, 2021.
- [40] S. Khandaker, Y. Toyohara, G. C. Saha, M. R. Awual, and T. Kuba, “Development of synthetic zeolites from bio-slag for cesium adsorption: kinetic, isotherm and thermodynamic studies,” *Journal of Water Process Engineering*, vol. 33, Article ID 101055, 2020.
- [41] H. Lei, Y. Muhammad, K. Wang et al., “Facile fabrication of metakaolin/slag-based zeolite microspheres (M/SZMs) geopolymer for the efficient remediation of  $\text{Cs}^+$  and  $\text{Sr}^{2+}$  from aqueous media,” *Journal of Hazardous Materials*, vol. 406, Article ID 124292, 2021.
- [42] Q. Tian and K. Sasaki, “Application of fly ash-based materials for stabilization/solidification of cesium and strontium,” *Environmental Science and Pollution Research*, vol. 26, no. 23, pp. 23542–23554, 2019.
- [43] G. Bar-Nes, O. Klein-BenDavid, L. Chomat, N. Macé, M. Arbel-Haddad, and S. Poyet, “Sr immobilization in irradiated Portland cement paste exposed to carbonation,” *Cement and Concrete Research*, vol. 107, pp. 152–162, 2018.
- [44] E. Johan, T. Yamada, M. W. Munthali, P. Kabwadza-Corner, H. Aono, and N. Matsue, “Natural zeolites as potential materials for decontamination of radioactive cesium,” *Procedia Environmental Sciences*, vol. 28, pp. 52–56, 2015a.
- [45] E. Johan, K. Yoshida, M. W. Munthali, N. Matsue, Y. Itagaki, and H. Aono, “Adsorption characteristics of  $\text{Cs}^+$  onto artificial zeolites synthesized from coal fly ash and diatomite,” *Journal of the Ceramic Society of Japan*, vol. 123, no. 1444, pp. 1065–1072, 2015b.
- [46] M. Arbel Haddad, E. Ofer-Rozovsky, G. Bar-Nes et al., “Formation of zeolites in metakaolin-based geopolymers and their potential application for Cs immobilization,” *Journal of Nuclear Materials*, vol. 493, pp. 168–179, 2017.
- [47] J. Kotatkova, J. Zatloukal, P. Reiterman, and K. Kolar, “Concrete and cement composites used for radioactive waste deposition,” *Journal of Environmental Radioactivity*, vol. 178–179, pp. 147–155, 2017.
- [48] Z. Xu, Z. Jiang, D. Wu et al., “Immobilization of strontium-loaded zeolite A by metakaolin based-geopolymer,” *Ceramics International*, vol. 43, no. 5, pp. 4434–4439, 2017.